



This is a repository copy of *Using nanoscopy to probe the biological activity of antimicrobial leads that display potent activity against pathogenic, multidrug resistant, gram-negative bacteria.*

White Rose Research Online URL for this paper:
<https://eprints.whiterose.ac.uk/144978/>

Version: Accepted Version

Article:

Smitten, K.L., Southam, H.M., de la Serna, J.B. orcid.org/0000-0002-1396-3338 et al. (5 more authors) (2019) Using nanoscopy to probe the biological activity of antimicrobial leads that display potent activity against pathogenic, multidrug resistant, gram-negative bacteria. *ACS Nano*, 13 (5). pp. 5133-5146. ISSN 1936-0851

<https://doi.org/10.1021/acsnano.8b08440>

This document is the Accepted Manuscript version of a Published Work that appeared in final form in *ACS Nano*, copyright © American Chemical Society after peer review and technical editing by the publisher. To access the final edited and published work see <https://doi.org/10.1021/acsnano.8b08440>

Reuse

Items deposited in White Rose Research Online are protected by copyright, with all rights reserved unless indicated otherwise. They may be downloaded and/or printed for private study, or other acts as permitted by national copyright laws. The publisher or other rights holders may allow further reproduction and re-use of the full text version. This is indicated by the licence information on the White Rose Research Online record for the item.

Takedown

If you consider content in White Rose Research Online to be in breach of UK law, please notify us by emailing eprints@whiterose.ac.uk including the URL of the record and the reason for the withdrawal request.



eprints@whiterose.ac.uk
<https://eprints.whiterose.ac.uk/>

Using Nanoscopy to Probe the Biological Activity of Antimicrobial Leads that Display Potent Activity Against Pathogenic, Multi-drug Resistant, Gram-negative Bacteria.

Kirsty Smitten,¹ Hannah M Southam*,² Jorge Bernardino de la Serna,^{3,4} Martin R Gill,^{1,5} Paul J Jarman,⁶ Carl G W Smythe,⁶ Robert K Poole*,² and Jim A Thomas*¹

^{†1}Department of Chemistry, The University of Sheffield, Western Bank, Sheffield S3 7HF, UK

²Department of Molecular Biology and Biotechnology, The University of Sheffield, Western Bank, Sheffield S10 2TN, UK

³Central Laser Facility, Rutherford Appleton Laboratory, Research Complex at Harwell, Science and Technology Facilities Council, Harwell-Oxford, Didcot OX11 0QX, United Kingdom

⁴Department of Physics, King's College London, London, WC2R, UK.

⁵Current address: CRUK/MRC Oxford Institute for Radiation Oncology, Department of Oncology, University of Oxford, Oxford, UK

⁶Department of Biomedical Science, The University of Sheffield, Western Bank, Sheffield S10 2TN, UK

ABSTRACT: Medicinal leads that are also compatible with imaging technologies are attractive as they facilitate the development of therapeutics through direct mechanistic observations at the molecular level. In this context, the uptake and antimicrobial activities of several luminescent dinuclear Ru^{II} complexes against *E. coli* were assessed and compared to results obtained for another ESKAPE pathogen, the Gram-positive major opportunistic pathogen *Enterococcus faecalis*, V583. The most promising lead displays potent activity, particularly against the Gram-negative bacteria, and potency is retained in the uropathogenic multi-drug resistant EC958 ST131 strain. Exploiting the inherent luminescent properties of this complex, super-resolution STED nanoscopy was used to image its initial localization at/in cellular membranes and its subsequent transfer to the cell poles. Membrane damage assays confirm that the complex disrupts the bacterial membrane structure before internalization. Mammalian cell culture and animal model studies indicate that the complex is not toxic to eukaryotes, even at concentrations that are several orders of magnitude higher than its minimum inhibitory concentration (MIC). Taken together, these results have identified an entirely new lead molecular architecture for hard-to-treat, multi-resistant, Gram-negative bacteria, which display activities that are already comparable to optimized natural product-based leads.

Although polypyridyl Ru(II) complexes have been much studied as imaging probes¹⁻⁷ and anti-cancer therapeutic leads,⁸⁻¹² initial biological studies focused on their potential as antimicrobials. In work that was in many ways before its time the Dwyer group demonstrated that lipophilic derivatives of [Ru(phen)₃]²⁺ (phen = 1,10 phenanthroline) containing methylated phen ligands are active against a range of bacteria, particularly Gram-positive species, which are unable to develop resistance to these structures.¹³⁻¹⁵ Since the minimum inhibitory concentrations (MIC) of these complexes were found to be relatively high compared to contemporary commercial antibacterials, this work was not further developed. However, in the modern context of a rapidly emerging global health crisis due to increasing antimicrobial resistance, AMR,¹⁶⁻¹⁹ the activity of such structures is being revisited.²⁰⁻²³

A notable example of these modern studies is the work of Collins and Keene on oligonuclear analogues of the structures first reported by Dwyer.²⁴ They found that tethering [Ru(phen)₃]²⁺ units together using flexible methylene-based linkers of different lengths produces complexes with considerably higher activity (lower MICs).^{25,26} The mechanism of activity for these compounds is still being explored. It has been hypothesized that they accumulate at ribosomes, causing condensation of polysomes,²⁷

but it has also been suggested that the cellular uptake and antibacterial activity of this class of compounds is due to their membrane-spanning ability.²⁸ However, except for one notable example involving a mononuclear complex,²⁹ these systems display lower activity against Gram-negative species such as *Escherichia coli*. Indeed, pathogenic Gram-negative species are a particularly pernicious AMR problem. For example in its recent report, the World Health Organization declared that a post-antibiotic era is “a very real possibility for the 21st century”³⁰ and identified Gram-negative *Pseudomonas aeruginosa*, *Acinetobacter baumannii*, and members of the *Enterobacteriaceae* that make up the majority of the ESKAPE group of serious hospital acquired infections³¹ as their three Priority 1 (Critical) pathogens in its “Priority Pathogens List For R&D”.³² The urgency of the situation is exacerbated by the lack of new therapeutic leads: no new class of antibiotics for Gram-negative pathogens has been approved for over 50 years and since 2010 only one new compound has entered the antibiotic pipeline through Phase 1 trials.³³ This situation has prompted calls to increase chemical diversity in the search for new leads.³⁴ It has also been suggested that the lack of completely new molecular “starting points leads” is the biggest roadblock for new antibiotic discovery.³⁵

In recent work the Thomas group have been exploring the application of dinuclear complexes as cell probes,^{5,36-38} therapeutics³⁹ and theranostics⁴⁰ in eukaryotic cells. Apart from producing live cell probes, this work has led to the identification of cytotoxic⁴¹ and photo-cytotoxic leads.^{42,43} In our original report on the cell uptake properties of 1^{4+} , we demonstrated through confocal microscopy that this complex was readily taken up by Gram-positive *Staphylococcus aureus*.³⁶ Given this fact, and the urgent need for new antimicrobial leads, we set out to investigate the therapeutic potential of related systems. In this report, we describe the luminescent derivatives of 1^{4+} , Figure 1, which display high activity against Gram-negative bacteria, including a pathogenic, globally disseminated, multidrug-resistant strain. We also show that the most active compound is taken up by cells through disruption of the bacterial cell wall, consequently specifically localizing at the poles of cells. Such studies are greatly facilitated by the fact that this compound is compatible with optical microscopy including super-resolution techniques.

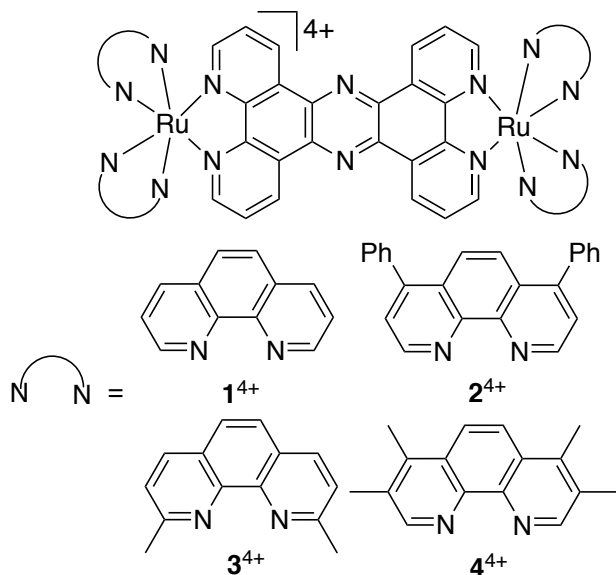


Figure 1. Structures of dinuclear Ru^{II} complexes relevant to this report

Results and Discussion

Cell-free studies

Previously reported complexes 1^{4+} and 2^{4+} were synthesized through established procedures.^{37,42} Inspired by the previous studies discussed above complexes 3^{4+} and 4^{4+} , incorporating methylated phen derivatives, were obtained and characterized through similar methods as hexafluorophosphate salts – see methods. Like their parent complexes, both 3^{4+} and 4^{4+} display the expected intense $Ru^{II} \rightarrow tpphz$ based 3MLCT emission in MeCN centred at 670 and 700 nm respectively. The biological properties of the four complexes were studied using their chloride salts, which were obtained by anion metathesis.

As many studies have demonstrated that the balance of lipophilicity and hydrophilicity is crucial for live-cell uptake of bioactive substrates,^{5,6,43,44} Log P for all four complexes were determined through octanol-water partition using the shake flask procedure – Table 1.

These data reveal that 2^{4+} is the only truly lipophilic complex. However, a comparison of Log P for 1^{4+} , 3^{4+} , and 4^{4+} indicates that relative lipophilicity increases with the number of methyl groups attached to the ancillary ligands of these complexes. Such small changes can have large effects on the cell uptake and bioac-

tivity of these complexes, an issue that was explored in live cell studies.

Table 1. Log P values for complexes 1^{4+} - 4^{4+}

Complex	Log P ^a
1^{4+}	-1.77
2^{4+}	1.03
3^{4+}	-1.38
4^{4+}	-1.13

^aLog octanol/water partition coefficients for each complex was determined after 20 h at 37°C

Bacterial studies

Uptake studies of 2^{4+} by the clinically critical Gram-negative bacteria found the compound was poorly soluble in complex aqueous media. This prompted us to design and investigate the uptake properties of two methylated compounds 3^{4+} and 4^{4+} .

In these studies, we chose to investigate the wild type K12-derivative MG1655 and uropathogenic multi-drug resistant EC958 ST131 strains of *E. coli* and, to aid comparison, we have also included another Gram-positive ESKAPE bacteria, the pathogenic gastrointestinal strain of *Enterococcus faecalis*, V583 (ATCC 700802), which is a major opportunistic pathogen and also a leading cause of urinary tract infections.

The minimum inhibitory concentration, MIC, of the four dinuclear complexes was obtained in both glucose defined minimal media (GDMM) and nutrient rich Mueller-Hinton-II (MH-II) as – whilst GDMM has been used in previous reported studies on metal complexes⁴⁵ – MH-II is closer to relevant biological conditions and is the bacterial growth medium recommended by the European Committee on Antimicrobial Susceptibility Testing. As demonstrated by the data summarized in Table 2, all four complexes show higher activity in GDMM.

Although the most lipophilic compound, 2^{4+} , shows the least activity – most likely due to its lower solubility in aqueous media – the lipophilic series of phen to TMP, shows an increase in lipophilicity and a concomitant increase in activity with 4^{4+} having the highest activity against all three strains of bacteria. This trend is consistent with the previous studies on the antimicrobial activity of polypyridyl Ru^{II} complexes.²⁵ Notably, 1^{4+} , 3^{4+} and 4^{4+} showed appreciable activity against the extended β -lactam-resistant strain of *E. coli*, and the vancomycin resistant strain of *E. faecalis*; complex 4^{4+} even displays higher activity than ampicillin against the wild type strain of *E. coli*. MIC data for the mononuclear parent compound ($[Ru(Phen)_2tpphz]^{2+}$), 5^{2+} , is provided for comparison – structure given in SI. The compound exhibits a much lower antimicrobial activity across all strains than its dinuclear derivatives; however the Gram-negative selectivity is still observed.

Table 2. MIC (μM) results for *E. coli* wild type (MG1655) and pathogenic (EC958) strains and *E. faecalis* pathogenic (V583) strain in GDMM and MH-II.

Complex	MG1655	EC958	V583
GDMM values			
1^{4+}	2.3	2.8	21.3
2^{4+}	7.8	10.4	64.0
3^{4+}	2.5	2.5	8.0

4 ⁴⁺	1.2	1.6	0.5
5 ²⁺	17.5	34.9	69.8
ampicillin	3.3	-	1.0
MH-II values			
1 ⁴⁺	12.9	14.7	64.0
2 ⁴⁺	139.9	145.1	64.0
3 ⁴⁺	6.8	6.8	42.7
4 ⁴⁺	5.6	5.6	3.3
5 ²⁺	139.7	279.5	279.5
ampicillin	5.7	-	0.5

Estimates of minimum bactericidal concentration, MBC, for 5²⁺ and 1⁴⁺ - 4⁴⁺ were also obtained and summarized in Table 3. These data show that, as for the MIC data, an increase in MBC values between GDMM and MH-II is observed. Again, 4⁴⁺ is the most active, and in GDMM its MBC values were lower than ampicillin, indicating that, for all strains of bacteria, it is more active than the conventional antibiotic. As with the MIC data, the mononuclear parent compound shows a weaker activity across all strains.

Table 3. MBC (μM) results for *E. coli* (MG1655, EC958 strains) and pathogenic *E. faecalis* (V583 strain) in GDMM and MH-II.

Complex	MG1655	EC958	V583
GDMM values			
1 ⁴⁺	11.0	4.6	53.3
2 ⁴⁺	15.5	25.9	85.3
3 ⁴⁺	20.3	5.1	53.3
4 ⁴⁺	2.4	2.4	4.0
5 ²⁺	34.9	17.5	279.5
ampicillin	11.4	-	6.3
MH-II values			
1 ⁴⁺	44.2	58.9	128.0
2 ⁴⁺	207.3	93.3	106.7
3 ⁴⁺	27.0	40.5	128.0
4 ⁴⁺	25.5	31.9	21.3
5 ²⁺	139.7	297.5	558.9
ampicillin	14.0	-	16.0

Having established that complex 4⁴⁺ had the most promising antibacterial properties, time-kill kinetics assays were carried out for both *E. coli* strains during 6 hours of exposure to increasing concentrations of the complex in minimal media at 37 °C - Figure 2.

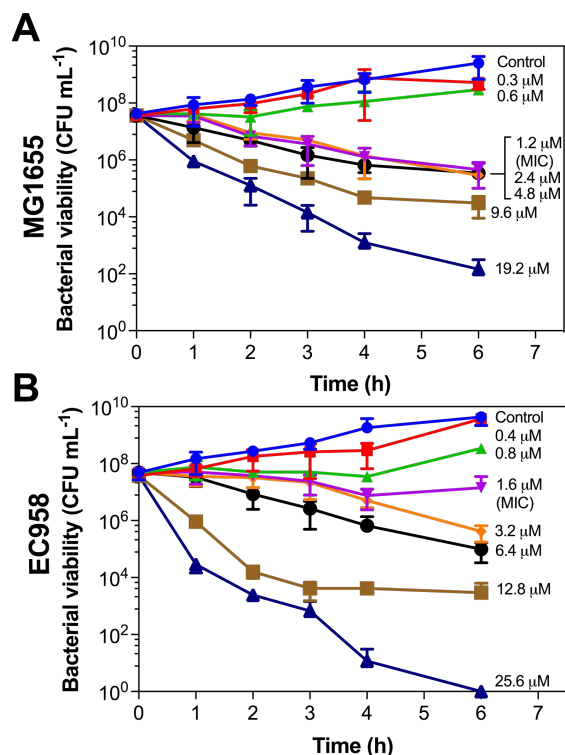


Figure 2. Complex 4⁴⁺ induces dose-dependent killing of *E. coli* MG1655 (A) and EC958 (B) planktonic cultures *in vitro*. The complex was added at various concentrations below and exceeding the MIC, 1.2 μM (A) or 1.6 μM (B), of 4⁴⁺ in GDMM. Killing was determined by monitoring the number of colony forming units (CFU) per mL at time intervals up to 6 h post treatment. Error bars represent three independent biological repeats \pm standard deviation (SD).

As might be expected, at concentrations lower than the MIC there was a gradual increase in colony forming units (CFU), as the bacteria continued to grow. In both strains, it is evident that, at concentrations of MIC and above, the compound halts the bacterial proliferation and reduces the number of viable bacterial cells. For EC958 at the highest exposure to 4⁴⁺ no colonies formed, showing that all bacteria within the system were killed. Discrepancies between MBC values and the time-kill assays may have arisen from different experimental conditions - the MBC assay involves stationary incubation over 16-18 hours, and the time kill assay is carried out with 90% aeration and rotation over 6 hours.

To investigate the uptake of 4⁴⁺ by *E. coli* cells, ICP-AES (Inductively-coupled plasma absorbance emission spectroscopy) studies were carried out. As previous research had demonstrated that 1⁴⁺ is actively transported into eukaryotic cells through an energy-dependent mechanism, uptake studies with 4⁴⁺ were carried out in the presence and absence of glucose - Figure 3. Experiments to investigate the accumulation of ruthenium in the *E. coli* EC958 over an hour were conducted as, at high concentrations, the time kill assays showed 99.9% of bacteria were killed within the first hour of exposure to 4⁴⁺. In these experiments, the concentration of iron, (a trace element in all cells) was also quantified as a control. It was found that on treatment with 4⁴⁺, iron content remained constant; furthermore, there was also a negligible change in CFU/mL, demonstrating that cells were not lysed during the accumulation experiment - Figure 4, SI.

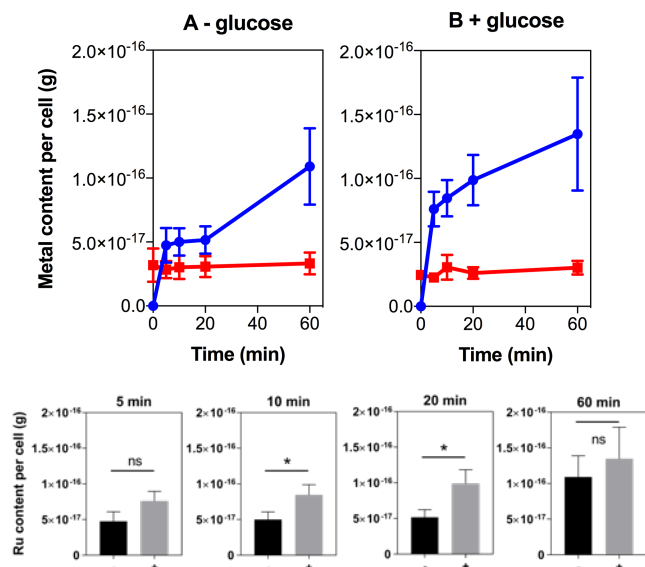


Figure 3. (I) ICP-AES data for the uptake of ruthenium by *E. coli* EC958 in the absence (A) and presence (B) of glucose after exposure to 4^{4+} . Ru (blue) and Fe (red) levels per cell are expressed as metal (g) per cell. Fe levels were calculated as a control. Conditions: concentration of 4^{4+} = 0.8 μ M. Cells were washed with 0.5%(v/v) nitric acid to remove unbound complex. Error bars represent three independent biological repeats \pm SD. (II) The difference in Ru content per cell (g) at each time point (+) with glucose and (-) without glucose. Showing significant differences in accumulation of ruthenium in the (+) with glucose sample at 10 and 20 minutes. Ruthenium content per cell determined *via* ICP-AES.

In glucose-free conditions, accumulation of 4^{4+} shows two phases: after an initial increase on exposure, low levels of ruthenium are maintained for about 20 min, after which uptake gradually doubles to a final figure of 1.1×10^{-16} g per cell. Assuming an average cell volume of $1 \mu\text{m}^3$,^{48,49} this is equivalent to an intracellular concentration of >1 mM. Contrastingly, in the presence of glucose - although the amount of ruthenium that finally accumulates is identical within experimental error - the uptake of the complex is rapid, with the maximum intracellular concentration of ruthenium being reached within 20 min. The significant differences between the glucose and glucose-free conditions are seen at 10 and 20 minutes.

The significant difference between experiments in the presence and absence of glucose at 10-20 min suggests that an energy-

dependent mechanism is - at least initially - involved in the active transport of 4^{4+} into cells. Furthermore, the discontinuity in uptake of the complex after 20 min in the absence of glucose, could suggest that the complex causes damage to cell membranes that facilitate its passive uptake. To explore these uptake issues in more detail, optical microscopy studies were then carried out.

It has been suggested that methods for direct molecular imaging of therapeutic leads will revolutionize the initial stages of drug development by providing evidence of biological activity and targeting capabilities.⁴⁶ It has also been hypothesized that the use of super-resolution techniques toward these goals will greatly improve target identification and facilitate high content screening.⁴⁷ Furthermore, as suitable imaging probes can provide high temporal and spatial resolution, they can be potentially used to directly identify the molecular mechanisms involving drug targets.⁴⁸ As we have recently demonstrated that 1^{4+} displays excellent compatibility with super resolution microscopy,⁴⁹ we extended this work to investigate the uptake and cellular response to exposure to 4^{4+} , thus providing an imaging study on prokaryote cells at super-resolution using a metal complex. Initially structured illumination microscopy^{50,51} was used to image the internalization of 4^{4+} at improved resolutions (~ 100 nm).

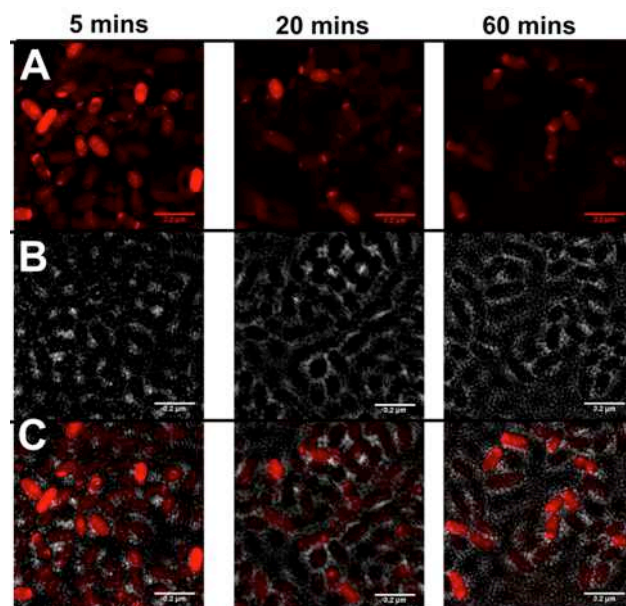


Figure 4. Localization of 4^{4+} in *E. coli* EC958 cells visualized through SIM at 5 min, 20 min, and 60 min. A: cells imaged using the emission of 4^{4+} on excitation at 450 nm using A568 filter B: phase contrast, C: combined image. After treatment with 0.8 μ M 4^{4+} , cells were washed with nitric acid before fixing with paraformaldehyde (16 v/v %).

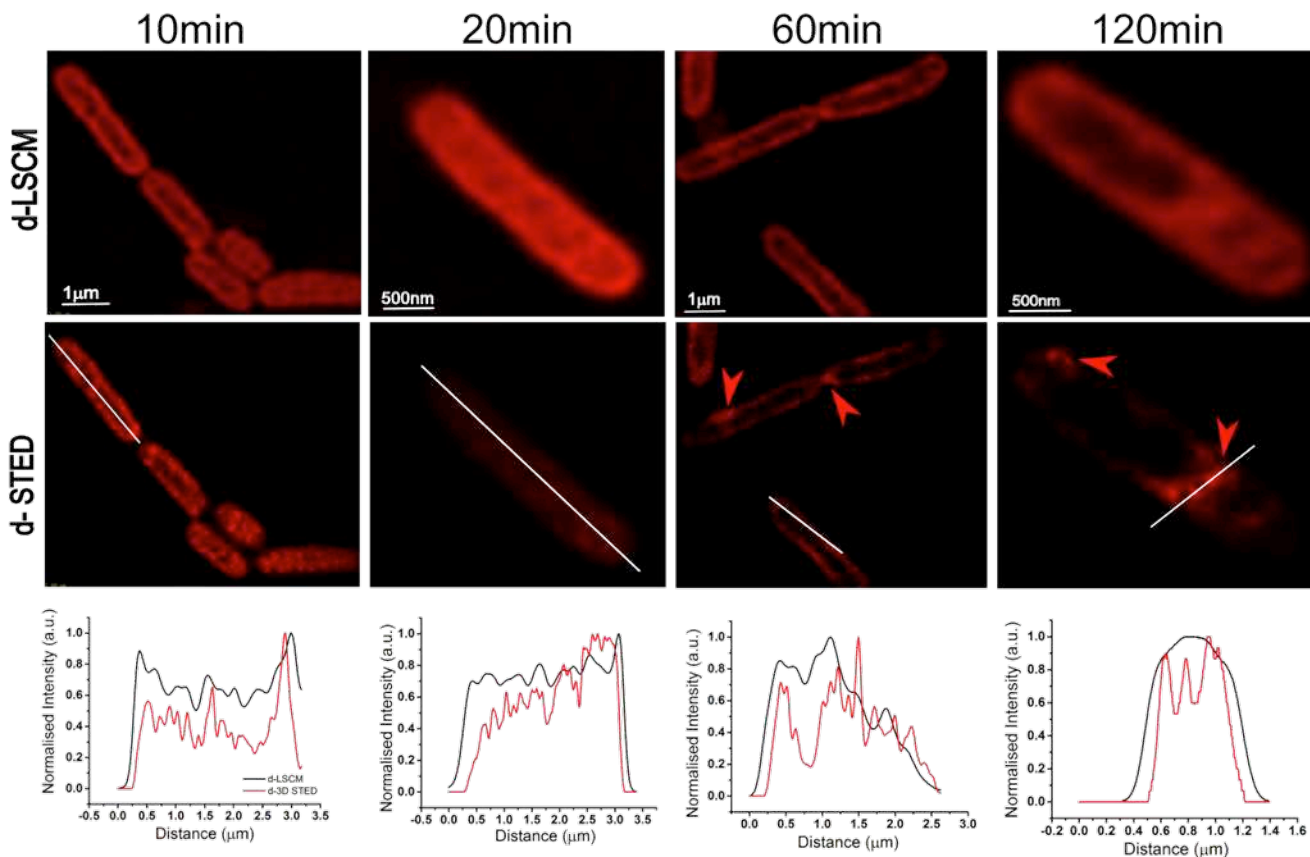


Figure 5. Localization of 4^{4+} in *E. coli* EC958 cells visualized through Laser Scanning Confocal Microscopy (LSCM) and Stimulated Emission Depletion (STED) nanoscopy at 5, 20, 60, and 120 min. Top row: cells imaged using the emission of 4^{4+} on excitation at 470 nm with a White Light Laser and a 470nm notch filter. Middle row: cells imaged with the same excitation and emissions settings; STED effect was obtained employing a 775nm depletion laser, and a 780nm vortex phase plate. Both deconvoluted diffraction-limited images (d-LSCM) and super-resolution (d-STED) images were processed using commercial Huygens software (SVI). The arrowheads highlight regions where 4^{4+} preferentially accumulates. Bottom row: normalised emission intensity profile along the solid white lines drawn on top of selected region of cells shown in the middle row; solid black lines represent the d-LSCM, solid red lines represent d-STED. Conditions: after treatment with $0.8 \mu\text{M } 4^{4+}$, cells were washed with nitric acid before fixing with paraformaldehyde (16%).

Consistent with the ICP-AES data, images obtained from the SIM studies indicated that 4^{4+} begins to internalize within bacteria after a 20 minute induction period - (Figure 4), prompting us to investigate this process at still higher resolutions.

Whilst stochastic super resolution techniques such as STORM offer exceptionally high resolutions, their extended image accumulation times make them less suited to monitoring dynamic processes. By contrast, stimulated emission depletion (STED) nanoscopy not only provides comparable sub-diffraction limited resolutions (down to 20nm) but, because it is a scanning based technique, it is also compatible with even live cell imaging.⁵²⁻⁵⁴ Therefore we used STED to image the uptake of 4^{4+} in exceptional detail (~50 nm) over a period of 5-120 minutes. Sample images taken over this time-course are shown in Figure 5.

To investigate whether changes in cell morphology occur within the first 5-20 min of exposure, images were taken at the same time points and identical conditions used in the accumulation experi-

ments. These images confirmed that 4^{4+} is readily and rapidly taken up by the pathogenic strain of *E. coli*. Interestingly, up to 20 min, the complex largely accumulates at cellular membranes and is generally distributed within the cell compartment, however, after this period it increasingly preferentially locates at the cell poles. This distinctive distribution has also been observed in *E. coli* cells treated with the tethered oligonuclear Ru^{II} complexes developed by Collins and Keene, and it has been attributed to localization within RNA-rich polysomes.²⁷

STED microscopy was also employed for detailed 3D sectioning experiments (3D STED). By employing a dual STED beam split into the XY plane and Z axis the highest possible 3D resolutions in each imaged plane was facilitated; a critical factor given the cellular dimensions of bacteria. Using this procedure, 3D STED resolutions of 50 nm in each plane and around 120 nm in the Z-axis were obtained.

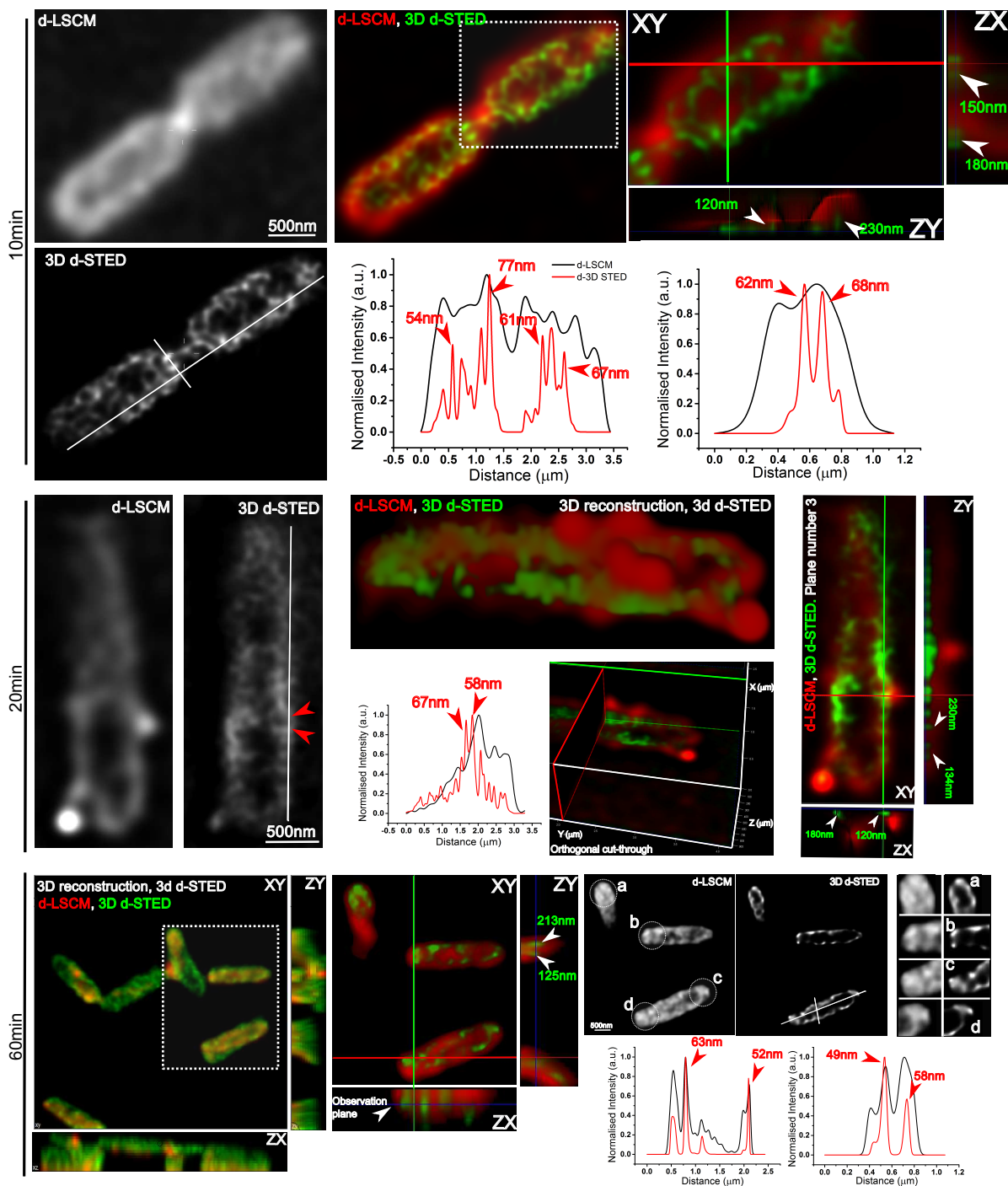


Figure 6. Representative images showing section planes of full-volume deconvoluted diffraction-limited cells and super-resolution images (d-LSCM and d-3D STED). Normalised emission intensity profile of the solid white lines drawn on top of selected region of cells are plotted. Solid black lines represent the d-LSCM, solid red lines represent d-3D STED. Zoomed-in areas of the dashed white squared drawn for each time point are shown adjacent to the images, as well as the orthogonal representation of every axis (XY, XZ, and YZ), where the increased resolution and better localization of 4^{4+} is shown in green. The 10 and 20 minute time points show accumulation at specific locations within the cell membrane; by the 60 minutes time point the compound localizes at sections of the cell poles as can be seen in the zoomed in regions (a,b,c,d). Conditions used are identical to those employed in Figure 3.

Figure 6 shows images taken at specific time points after exposure to 4^{4+} . During the first 10 min the probe accumulates within the cell membrane forming a distinctive distribution pattern, but after 20 minutes dye redistribution begins and accumulation at the poles becomes increasingly apparent. In addition, at 20 minutes changes in cell morphology are observed, with lumps appearing on the membrane.

Taken together with the ICP-AES data, the SIM and STED imaging studies indicate a change in the quality of uptake and intracellular distribution of the complex after around 20 min. Furthermore, as the molecular weight of 4^{4+} is considerably larger than the upper limit for porin-mediated uptake (~ 600 Da), this mechanism can be discounted.¹⁷ To investigate the possibility of mem-

brane damage a second co-staining experiment with the probe Alexa Fluor NHS-ester 405 was carried out - Figure 7.

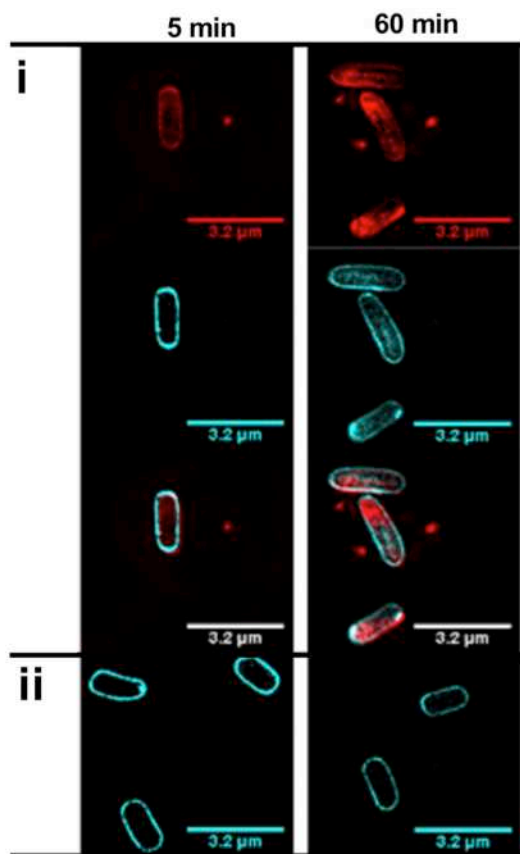


Figure 7. Co-localization of 4^{4+} and NHS-ester 405 in *E. coli* EC958 cells visualized through SIM at 5 min (left), and 60 min (right). i. Cells were treated with $0.8 \mu\text{M}$ 4^{4+} , then washed with nitric acid before fixing with paraformaldehyde (16%). After fixation cells were treated with $2.5 \mu\text{g/mL}$ of NHS-ester 405. Top panel: emission of 4^{4+} (A568 filter) middle panel: NHS-ester 405 emission at 405 nm (DAPI filter) Bottom panel: merged images. ii. Staining with NHS-ester in the absence of 4^{4+} .

Since Alexa Fluor NHS-ester 405 is impermeable to non-compromised bacterial membranes it localizes and images cell membranes. Following 5 min exposure to 4^{4+} , localization of NHS-ester 405 is - as expected - restricted to the cell membrane of bacteria. However, after 60 min exposure to the complex, both dyes are found to internalize within *E. coli*. In contrast, even after 60 min, cells solely stained with NHS-ester 405 continue exclusively to display membrane staining. The fact that the membrane stain is internalized only after treatment with 4^{4+} offers further evidence that the complex is disrupting the structure of bacterial membranes. To investigate this phenomenon more quantitatively, concentration-dependent ATP cellular leakage assays were performed.⁵⁵ Following treatment with specific concentrations of 4^{4+} , the presence of extracellular ATP, released from damage to bacterial cell membranes, was detected using the luminescence generated from the ATP-dependent reaction between recombinant firefly luciferase and D-luciferin.

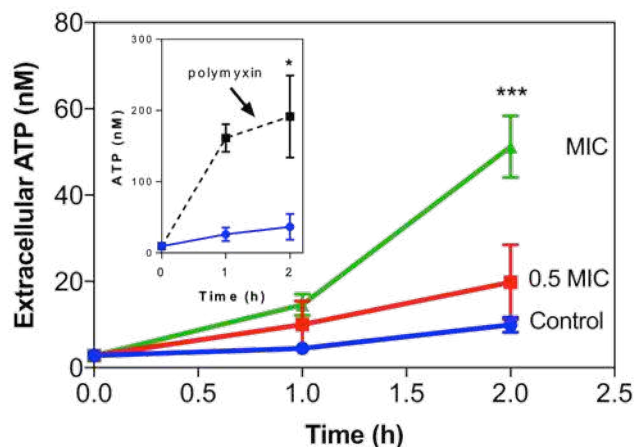


Figure 8. Determination of 4^{4+} -induced ATP released from *E. coli* EC958 cells. Extracellular [ATP] (nM) quantified with recombinant luciferase and D-luciferin, with ATP released measured on a luminometer for samples exposed to 0 (control), 0.8, 1.6 μM (MIC) of 4^{4+} over a period of two hours. A three-star significant difference is observed between 0 and 1 MIC, P value = 0.0006. Error bars represent three biological repeats \pm SD. Inset: ATP positive control - polmyxin $4 \mu\text{g/mL}$.

Data obtained from the luminescence-based determination of [ATP], summarized in Fig 8, confirm that bacterial membranes are compromised in a concentration-dependent manner on exposure to 4^{4+} . Given this effect it seems likely that the uptake of the complex in glucose-free conditions is biphasic, as membrane damage must initially occur before the level of internalized 4^{4+} can rise to high concentration. The significant ATP release, supported with the observation of membrane binding at the nanoscale and internalisation of NHS-ester signifies that membrane damage is the mechanism of therapeutic action

To further investigate this issue, the effect of 4^{4+} on membrane potential was studied using the dye DiOC₂(3). Following exposure to this complex, a shift in the intramolecular emission of the dye from green to red was observed when EC958 cells were treated at MIC concentration- Figure 7, SI. This shift in emission is associated with larger membrane potentials causing DiOC₂(3) to self-associate at higher cytosolic concentrations. Again, this observation indicates that 4^{4+} disrupts membrane function.⁵⁶

To understand the true extent of the membrane damage Transmission Electron Microscopy (TEM) was used to image structural changes induced by exposure to 4^{4+} - Figure 9.

E. coli EC958 cells were treated with 4^{4+} at concentrations below and at the MIC and then fixed and imaged at zero to two hours after exposure. As 4^{4+} contains two electron dense Ru^{II} moieties it functions as a TEM contrast agent in itself. In comparison to the control (0 minutes) the outer membrane is not clearly observed at the two later time-points.

In both treatment regimes after one hour exposure the majority of cells display visibly damaged membrane structures and blebbing of the membrane is observed in a number of cases. After two hours exposure the outer membrane (OM) is mostly detached resulting in a large amount of cell debris likely caused by cell lysis. These TEM images confirm the compound causes damage to both membranes.

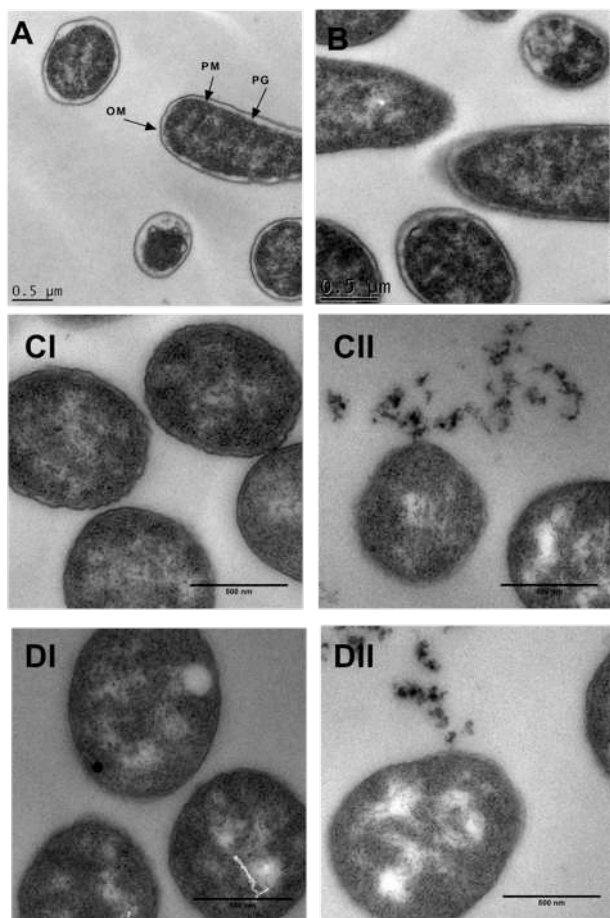


Figure 9. Localization of 4^{4+} in *E. coli* EC958 cells visualized through Transmission Electron Microscopy at 0 (A) and 10 minutes (B) at MIC concentration. Later time-point images at 1 (I) and 2 hours (II). After treatment with 0.5MIC (C) and MIC (D) concentrations of 4^{4+} . Directly using the complex as a contrast agent to show accumulation of 4^{4+} in the cell membrane. OM, peptidoglycan layer (PG) and plasma membrane (PM) are identified in AI. Cells were fixed with osmium tetroxide.

As 4^{4+} shows high antimicrobial activity and is membrane targeting, the potency of the compound in non-cancerous human cells was determined to further explore its potential as an antimicrobial theranostic lead. MTT-assays on the human embryonic kidney line, HEK293 revealed an average IC_{50} value of 135 μM , indicating at least an 80-fold magnitude difference in inhibitory concentration against bacteria and HEK293 cells – Table 4.

Table 4. Ratio of MIC (μM) and HEK293 IC_{50} values for each strain of bacteria.

Cell line	MIC (μM)	IC_{50}/MIC
<i>E. coli</i> EC958	1.6	84.4
<i>E. coli</i> MG1655	1.2	112.5
<i>E. faecalis</i> V583	0.5	270

Given the promising comparison between IC_{50} and MIC values an animal model screen was carried out. As many aspects of the physiology of *Galleria mellonella* larvae, particularly their immune system, are very similar to mammal they are much employed as an *in vivo* model,^{57,58} including as a toxicity screen,

^{59,60} yielding results that are comparable to commonly used mammalian models. A toxicity screen was conducted with 4^{4+} and Kaplan-Meier survival curves plotted - Figure 10.

All concentrations used were above the MIC for 4^{4+} against EC958, and within the daily dose range used in the clinic for antimicrobials. From Log-rank tests it was determined that there was no significant difference between the percentage survival with the *Galleria* treated with 4^{4+} and the control at all compound concentrations. In addition, activity and melanisation scores showed that there was no significant negative effects on the *Galleria* exposed to 4^{4+} , confirming that this compound is not toxic at concentrations well above the MIC.

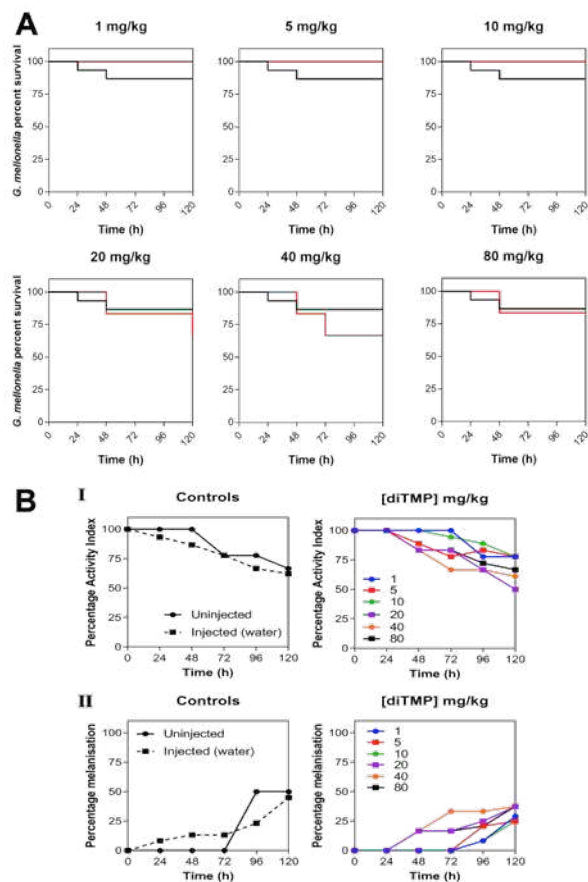


Figure 10. (A) *Galleria mellonella* toxicity screen Kaplan-Meier survival curves, cells treated with 0-80 mg/kg of $[4^{4+}]Cl_4$, incubated at 37.5 °C for 120 hours – control (black), compound (red). (B) (I) Activity score data from the *Galleria* collected every 24 hours for 120 hours, experimental determination of the activity scores given in the experimental section of the SI. (II) Melanisation score data from the *Galleria* study, experimental determination of the melanisation scores given in the experimental section of the SI.

Conclusions

Faced by the challenges presented by the emergence and rapid increase in multi-resistant bacterial infections, recent reports have highlighted the need to develop radically new approaches toward the discovery of antibiotics.^{18,31,61-63} In the context of the failure of traditional high throughput screening, there has also been a call to sample new chemical spaces in the hope of identifying leads with novel activity,^{31,34,61,64-66} that function through multiple mechanisms³⁵ and/or target and disrupt membranes.⁶⁷

Although mononuclear transition metal complexes and oligonuclear complexes linked by flexible tethers have been investigated, there has been little work on dinuclear systems linked by a rigid extended aromatic bridging ligand, an architecture that offers particular merits for activity against Gram negative bacteria. Previous reports have highlighted the distinctive biophysical properties a species must possess to be active against Gram-negative pathogens,⁶⁸⁻⁷⁰ indicating that - compared to typical drug architectures - active systems should be more complex 3-D structures, polar, possess potentially ionizable nitrogen sites, and be rigid. Furthermore, it has been suggested the poor hit rate for discovery is due to a lack of more polar systems in high throughput screening libraries.⁶⁹ As the systems discussed in this report meet all the above criteria it is perhaps not surprising that they display such promising activity. Given that no significant new organic antibiotic that is selectively effective against Gram-negative bacteria has been developed in the past five decades, this study provides further evidence that there is considerable potential in exploiting the Ru^{II} coordination sphere as a 'chemical space' for the generation of novel antimicrobial structures. This is further illustrated by the fact that the systems described herein are already considerably more active than recently reported natural product analogues that were optimized as Gram-negative therapeutic leads.⁷¹

It is possible that the therapeutic mechanism of complex **4**⁴⁺ solely involves its membrane targeting properties; although - once internalized - it localizes and binds at specific regions within cells, suggesting a second cellular target. Indeed as pathogenic, therapeutically-resistant, strains of *E. coli* are still sensitive to the complex, it seems likely that the membrane disruption effect of **4**⁴⁺ may only be one facet of a more complex set of interactions and cellular responses.

Future studies will fully delineate the action of the compounds at a molecular scale. For example, as uptake appears to take place by both energy-dependent and -independent mechanisms, work to identify how membrane disruption occurs is underway. The biological significance of localization of **4**⁴⁺ at the poles of the cell compartment, which may also be basis of the apparent selectivity towards Gram-negative species, is also being investigated. All these studies will be facilitated by the fact that such systems are simultaneously excellent imaging agent for super resolution microscopy techniques and TEM, allowing sub-cellular localization, molecular targeting, and therapeutic action to be directly probed.^{36,49}

Methods

Chemistry Methods

The ligand tpphz was synthesized using a reported procedure.⁴²

[Ru(N-N)₂Cl₂]⁷²

Four compounds were synthesised by the following method, where N-N represents the substituted phenanthroline ancillary ligand. RuCl₃·3H₂O, N-N and LiCl were heated in DMF for 8 hours under reflux. The reaction mixture was cooled to room temperature and acetone added. This was stored at 4 °C for 16 hours. The dark purple precipitate was washed with water and ethanol and dried in vacuo.

[Ru(1,10-phenanthroline)₂Cl₂]

RuCl₃·3H₂O (1.56 g, 6 mmol), LiCl (1.55 g, 36.9 mmol), phen (2.5 g, 13.9 mmol), DMF (20 mL) and acetone (100 mL). Mass = 2.41 g (4.59 mmol, 66.1 % yield). ES-MS m/z (%): 497 (70) [M-Cl]⁺, 525 (100) [M-Cl]⁺+CO.

[Ru(4,7-diphenyl-1,10-phenanthroline)₂Cl₂]

RuCl₃·3H₂O (1.05 g, 4.15 mmol), DIP (2.3 g, 6.92 mmol), LiCl (1.04 g, 24.50 mmol), DMF (18 mL) and acetone (100 mL) Mass = 2.15 g (2.59 mmol, 68.9 % yield) black-purple crystal solid. MS m/z (%): 801.0 (15) [M-Cl]⁺, 829.0 (100) [M]⁺. Carbon monoxide displaced one of the chlorines.

[Ru(2,9-dimethyl-1,10-phenanthroline)₂Cl₂]

RuCl₃·3H₂O (1.56 g, 6 mmol), LiCl (1.55 g, 36.9 mmol), DMP (phenanthroline (2.5 g, 12 mmol), DMF (20 mL), acetone (100 mL). Mass = 2.32 g (3.99 mmol, 66.6 % yield). ES-MS m/z (%): 552.9 (100) [M-Cl]⁺, 580.9 (100) [M-Cl]⁺+CO.

[Ru(3,4,7,8-tetramethyl-1,10-phenanthroline)₂Cl₂]

RuCl₃·3H₂O (1.14 g, 5.50 mmol), TMP (2.4 g, 10.16 mmol), LiCl (1.47 g, 34.68 mmol), DMF (19 mL) and acetone (100 mL). Mass = 2.07 g (3.21 mmol, 63.2 % yield) purple solid. MS m/z (%): 609.1 (62) [M-Cl]⁺, 637.1 (100) [M]⁺ 667.1 (44) [M+Na]⁺. Carbon monoxide displaced one of the chlorines.

[{Ru(N-N)₂}₂(tpphz)][PF₆]₄

The four compounds were synthesized by the following general procedure.⁷³ [Ru(N-N)₂Cl₂] and (tpphz) were added to a 1:1 solution of ethanol and water. The solution was heated at reflux for 12 hours under nitrogen. After completion the reaction mixture was cooled to room temperature and stored at 4 °C for 16 hours. The red solution was filtered and the ethanol removed by rotary evaporation. A saturating amount of NH₄PF₆ was added; this caused the formation of a dark red precipitate. The precipitate was collected by filtration, washed with water and recrystallized in acetonitrile by addition of diethyl ether. The product was dried *in vacuo* and purified on an alumina column, using the following solvent system: was 95% MeCN, 3% dH₂O and 2% KNO₃.

[{Ru(1,10-phenanthroline)₂}₂(tpphz)][PF₆]₄

Tpphz (0.263g, 0.68 mmol), [Ru(phen)₂Cl₂] (1g, 1.89 mmol) and ethanol/water (50 mL). Mass = 1.1 g (0.58 mmol, 85.6 % yield). ¹H NMR (MeCN-d₆) δ (splitting integration): 7.71 (m, 8H), 7.94 (dd, 4H), 8.09 (d, 4H), 8.29 (dd, 8H), 8.33 (s, 8H), 8.69 (dd, 8H), 10.01 (dd, 4H). ES-MS; m/z (%): 799 (10) [M-2PF₆]²⁺, 484 (15) [M-3PF₆]³⁺, 321 (50) [M-4PF₆]⁴⁺. Accurate mass analysis: C₇₂H₂₈N₁₄[¹⁰²Ru]₂⁴⁺ Calculated 321.1110. Found 321.1112.

[{Ru(4,7-diphenyl-1,10-phenanthroline)₂}₂(tpphz)][PF₆]₄

[Ru(DIP)₂Cl₂] (1.47 g, 1.76 mmol), tpphz (0.234 g, 0.61 mmol) and ethanol/water (80 mL). Mass = 1.21 g (0.48 mmol, 78.7 %) red-brown solid. ¹H NMR (MeCN-d₆) δ (splitting integration): 7.66 (m, 40H), 7.7 (d, 8H), 8.0 (dd, 4H), 8.27 (s, 8H), 8.3 (d, 4H), 8.4 (dd, 4H), 8.5 (d, 4H), 10.0 (d, 4H). MS; m/z (%): 1103 (35) [M-2(PF₆)]²⁺, 687 (88) [M-3(PF₆)]³⁺, 479 (56) [M-4(PF₆)]⁴⁺. 7.7 (m, 40H), 7.84 (d, 4H), 7.81 (dd, 4H), 8.1 (dd, 4H), 8.4 (s, 8H), 8.68 (d, 4H), 8.74 (dd, 8H), 10.2 (d, 4H). Accurate mass analysis: C₁₂₀H₇₆N₁₄[¹⁰²Ru]₂⁴⁺ Calculated 479.1111. Found 479.1110. Elemental analysis [{Ru(DIP)₂}₂(tpphz)] (NO₃)₄·10H₂O, C₁₂₀H₉₆N₁₈O₂₂Ru₂: Calcd: C; 61.48, H; 4.12, N; 10.75. Found: C; 61.83, H; 4.36, N; 10.50.

[{Ru(2,9-dimethyl-1,10-phenanthroline)₂}₂(tpphz)][PF₆]₄

Tpphz (0.263 g, 0.68 mmol), [Ru(dmp)₂Cl₂] (1.02 g, 1.73 mmol) and ethanol/water (50 mL). Mass = 0.98 g (0.49 mmol, 72 % yield). ¹H NMR (MeCN-d₆) δ (splitting integration): 2.34 (s, 24H), 7.30 (d, 4H), 7.59 (m, 8H), 7.90 (d, 4H), 8.20 (d, 4H), 8.37 (t, 8H), 8.83 (d, 4H), 9.80 (d, 4H). ES-MS; m/z (%): 855 (8) [M-

2PF₆)²⁺, 522 (70) [M-3PF₆)³⁺, 355 (10) [M-4PF₆)⁴⁺, Accurate mass analysis: C₈₀H₅₂N₁₄[¹⁰²Ru]₂⁴⁺ Calculated 355.1111. Found 355.1112. Elemental analysis for [Ru(DMP)₂]₂(tpphz)(PF₆)₄·2H₂O, C₈₀H₆₄F₂₄N₁₄O₂P₄Ru₂: Calcd: C; 47.21, H; 3.17, N; 9.63. Found: C; 46.09, H; 3.17, N; 9.71.

[Ru(3,4,7,8-tetramethyl-1,10-phenanthroline)₂]₂(tpphz)[PF₆]₄

[Ru(TMP)₂Cl₂] (1.12 g, 1.73 mmol) and tpphz (0.260 g, 0.68 mmol), water/ethanol (80 mL). Mass = 1.22 g (0.58 mmol, 85.7 % yield). MS; m/z (%): 911 (10) [M-2(PF₆)²⁺, 559 (100) [M-3(PF₆)³⁺. ¹H NMR (MeCN-d₆) δ (splitting integration): 2.1 (s, 4H), 7.8 (s, 4H), 7.9 (t, 8H), 8.2 (dd, 4H), 8.4 (s, 8H), 9.9 (dd, 4H). ¹H NMR (Acetone-d₆) δ (splitting integration): 2.1 (dt, 48H), 8.0 (m, 4H), 8.1 (s, 4H), 8.2 (s, 4H), 8.52 (d, 4H), 8.6 (s, 8 H), 10.1 (d, 4H). Elemental analysis [Ru(3, 4, 7, 8-Tetramethyl-1,10-phenanthroline)₂]₂(tpphz) (PF₆)₄·5.5H₂O, C₈₈H₈₇N₁₄O_{5.5}Ru₂P₄F₂₄ Calculated: C; 47.93, H; 3.97, N: 8.89. Found C; 47.92, H; 3.83, N; 8.82. Accurate mass analysis: C₈₈H₇₆N₁₄[¹⁰²Ru]₂⁴⁺ Calculated 383.1111. Found 383.1112.

[Ru(1,10-phenanthroline)₂](DPQ)[PF₆]₂

[Ru(Phen)₂Cl₂] (1.01 g, 1.90 mmol), DPQ (0.495 g, 2.36 mmol) and EtOH:H₂O (50 mL). Mass = 0.910 g (0.946 mmol, 49.8 %). MS (TOF MS LD+) m/z (%): 671 (100) [M-2PF₆)²⁺, 817 (50) [M-PF₆)⁺. ¹H NMR (DMSO-d₆) δ (splitting integration): 7.52 (2H, dd), 7.63 (2H, dd), 7.85 (2H, dd), 7.94 (4H, dd), 8.30 (4H, q), 8.37 (2H, dd), 8.51 (2H, dd), 8.62 (2H, dd), 8.73 (2H, dd).

[Ru(Phen)₂(tpphz)][PF₆]₂

5,6-diamino-1,10-phenanthroline (100 mg, 0.48 mmol), hot methanol (20 mL), [Ru(Phen)₂DPQ][PF₆]₂ (650 mg, 0.71 mmol), acetonitrile (30 mL). Mass = 0.251 g (0.221 mmol, 31.1%). ¹H NMR (CD₃CN-d₆) δ (splitting integration): 7.76 (8H, m), 8.19 (4H, dd), 8.34 (4H, dd), 8.68 (4H, t), 8.80 (2H, d), 9.43 (4H, dd). MS; m/z (%): 991.4 [M-PF₆)⁺ (100); 845.4 [M-2PF₆)⁺ (35); 423.2 [M-2PF₆)²⁺ (25). C₄₈H₂₈N₁₀[¹⁰²Ru]₂²⁺ Calculated 423.0765. Found 423.0783.

Anion metathesis

The hexafluorophosphate salt of each complex was dissolved in the minimum volume of acetone and a saturated solution of tetrabutylammonium chloride in acetone added. The resultant precipitated chloride salt was collected by filtration, washed with cold acetone and dried in vacuo.

Absorption spectra

An emission quartz cuvette was loaded with varying concentrations of the [Ru(TMP)₂(tpphz)] chloride salt dissolved in water (0-20 μM). Each reading was baseline corrected. The absorption spectra at 200-800 nm were obtained with a Cary 500 Scan UV-vis-NIR Spectrophotometer, set to double beam mode (spectral band width = 2 nm), with a medium scan speed of 600 nm min⁻¹.

Molar extinction coefficients

Molar extinction coefficients were calculated using the Beer-Lambert law. They were calculated from a plot of measured absorbance against sample concentration.

$$A = \epsilon cl \quad \text{Equation 5.1: Beer-Lambert Law}$$

Excitation and emission spectra

A fluorescence quartz cuvette was loaded with varying concentration of the [Ru(TMP)₂(tpphz)]²⁺ chloride salt dissolved in water

(0-20 μM). The excitation and emission spectra were recorded using a Fluoromax-3 Spectrophotometer, slit width 5 nm, scan speed 100 nm min⁻¹. The emission spectra were taken at the 424 nm peak seen in the absorption spectra.

Determination of LogP

Relative lipophilicities or partition coefficients of 1⁴⁺ - 4⁴⁺ across 1-octanol and H₂O (logP_{oct/wat}) were determined via the shake-flask method.⁷⁴ Aqueous stocks of 1⁴⁺ - 4⁴⁺ were prepared at 200 and 300 μg mL⁻¹ were added to equal volumes of 1-octanol that had been pre-saturated with H₂O for 36 h. After incubation with shaking at 37 °C for 24 h, the 1-octanol and aqueous phases were recovered and the relative distribution of each compound was determined by UV-vis absorbance spectroscopy at 430 – 455 nm.

Microbiology and Microscopy Methods

Bacterial strain information and general growth procedures

Microbiological studies were conducted with: (1) wild-type K-12 derivative laboratory strain *Escherichia coli* MG1655; (2) CTX-M-15 type extended spectrum β-lactamase (ESBL)-producing clinical isolate *E. coli* EC958 (ST131)⁷⁵ and (3) *Enterococcus faecalis* vancomycin-resistant V583 clinical isolate (ATCC 700802).⁷⁶ Bacteria were routinely grown under aseptic, aerobic conditions in autoclave-sterilised culture medium at 37 °C. Lyso-geny Broth (LB) (Formedium), Mueller-Hinton II (MH-II) (Sigma-Aldrich) and Brain-Heart Infusion (BHI) (Sigma-Aldrich) were prepared as per manufacturers' instructions. Glucose defined minimal medium (GDMM) was prepared by dissolution of 4 g L⁻¹ K₂PO₄, 1 g L⁻¹ KH₂PO₄, 1 g L⁻¹ NH₄Cl, 10 mg L⁻¹ CaCl₂ and 2.6 g L⁻¹ K₂SO₄ in deionized H₂O with supplementation of 10 mL L⁻¹ Trace Elements solution. The pH was adjusted to 7.4 by the addition of NaOH. GDMM was sterilised by autoclaving and then further supplemented with 1 mM MgCl₂ and 20 mM glucose prior to growth studies. Trace elements contained 5 g L⁻¹ ethylenediaminetetraacetic acid (EDTA), 0.5 g L⁻¹ Fe(III)Cl₃·6H₂O, 50 mg L⁻¹ ZnO, 10 mg L⁻¹ CuCl₂·2H₂O, 10 mg L⁻¹ CoNO₃·6H₂O, 10 mg L⁻¹ H₃BO₃, 0.12 mg L⁻¹ (NH₄)₂MoO₄ and 17 mg L⁻¹ Na₂O₄Se.

Prior to experiments, bacterial starter cultures were prepared by inoculating LB (*E. coli*) or BHI (*E. faecalis*) with a single colony of bacteria and then grown for overnight at 37 °C with shaking for 16 – 18 h. For *E. coli* EC958 and *E. faecalis* V583, starter cultures were additionally supplemented with 50 μg mL⁻¹ ampicillin or 10 μg mL⁻¹ vancomycin. Starter cultures were washed once and re-suspended in the appropriate growth medium for each experiment. For short-term storage, bacterial stocks were maintained on nutrient agar plates at 4 °C for 2 – 3 weeks. For long-term storage, strains were stored as cell suspensions in 30 % (v/v) LB 70 % (w/v) glycerol at – 70 °C.

Determination of Minimum Inhibitory Concentrations (MICs) and Minimum Bactericidal Concentrations (MBCs)

MICs and MBCs of 1⁴⁺ - 4⁴⁺ and ampicillin (comparison) were determined via the standard broth-dilution method in 96-well microtitre plates in either MH-II, as recommended by European Committee of Antimicrobial Susceptibility Testing (EUCAST) or in GDMM. For *E. faecalis*, both media were further supplemented with 10 % (v/v) BHI to facilitate growth. The MIC of each compound was evaluated using 2-fold increasing concentrations of each compound between 2 - 512 μg mL⁻¹ against a bacterial inoculum of 10⁷ – 10⁹ colony forming units per mL (CFU mL⁻¹), corresponding to an optical density at 600 nm (OD₆₀₀) of 0.05 – 0.075. Plates were incubated at 37 °C for 20 h. After this time, the level of turbidity in each well was used to determine the extent

bacterial cell growth in the presence of the compounds. The minimal concentration of compound that did not permit bacterial growth was determined to be the MIC. For MBC determination, 10 μ L samples of each well were then transferred to nutrient agar plates and further incubated at 37 °C. The lowest concentration of compound in which no CFU were observed after plating was determined to be the MBC. MIC/MBCs were determined from 3 independent biological repeats.

Cytotoxicity MTT assays

Yellow MTT (3-(4,5-dimethylthiazol-2-yl)-2,5-diphenyltetrazolium bromide) is reduced to a purple formazan product in the mitochondria of living cells by reductase enzymes. The reduction of MTT can only occur within active mitochondria, therefore the amount of formazan produced is directly related to the number of viable cells in the sample. In this experiment the amount of formazan was quantified by absorbance between 500-600 nm, the toxicity of the compound was deduced by comparison of formazan content for cells exposed to the compound and those in the untreated control.

IC₅₀ values

Cell cultures were grown on 24 or 48 well plates and allowed to grow for 24 hours. Cell cultures were then treated with solutions of the Ru(II) complex at various concentrations (10% PBS: 90% medium) for the given incubation time in triplicate. Solutions were removed and the cells incubated with 0.5 mg ml⁻¹ MTT dissolved in PBS for 30-40 minutes. The formazan product was eluted using 200 μ l/well of acidified propan-2-ol, 150 μ l of this was transferred to a 96 well plate and the absorbance quantified by spectrophotometer (540 nm, referenced at 640 nm). An average absorbance for each concentration was obtained and cell viability was determined as a percentage of untreated negative control wells (10% PBS: 90% medium). Using Sigmaplot 11.0 software, a 3 parameter sigmoidal curve was used to fit each data set ($R^2 > 0.97$ for each fit) and the IC₅₀ value (the concentration corresponding to 50% viability) calculated by interpolation.

Time-kill assays

E. coli MG1655 and EC958 strains were grown on GDMM to early exponential phase, diluted to approximately 10⁸-10⁹ CFU mL⁻¹ and 4⁺ was added at 0 – 25.6 μ M (0 - 8 x MIC). Immediately prior to TMP addition, and at 1-6 h thereafter, culture growth (turbidity at OD₆₀₀) and viability (CFU mL⁻¹) were measured. Cell viability was determined via the standard viable counts method, which is based on the ability of a single viable bacterial cell to form a colony when grown on agar plates. 10-fold serial dilutions of cell culture samples were prepared in sterile PBS and then 3 x 10 μ L of each dilution was spotted onto nutrient agar plates. Plates were then incubated overnight at 37 °C to permit colony growth and cell viability was determined as the average number of counted CFU mL⁻¹. Time-kill assays were performed as three independent biological repeats.

Uptake of 4⁺ by *E. coli* and determination of cellular ruthenium and iron levels

Uptake and cellular accumulation of 4⁺ by *E. coli* EC958 was determined by measuring bacterial cell metal content by Inductively Coupled Plasma-Atomic Emission Spectroscopy (ICP-AES) as follows. *E. coli* EC958 cultures were grown to mid-exponential phase in LB broth, washed in PBS and then resuspended in PBS +/- 20 mM glucose to approximately 10⁸-10⁹ CFU mL⁻¹. 4⁺ was added to cells at MIC level (1.6 μ M) and then 20

mL samples of culture were harvested at 5, 10, 20 and 60 min after 4⁺ addition. Samples of non-4⁺ treated cells were also taken for comparison. Samples were centrifuged at 5,000 x g for 20 min at 4 °C to obtain cell pellets and the supernatant containing unbound extracellular 4⁺ was discarded. The resultant cell pellets were then washed twice in 0.5 % (v/v) Aristar nitric acid to remove loosely bound residual 4⁺. To prepare cell material for ICP-AES, cell pellets were resuspended in 0.5 mL Aristar nitric acid (69 % (w/v) and then placed in a sonicator bath for 30 min to completely dissolve cells. The resulting digest was then diluted to a final volume of 5 mL with diluted nitric acid and then samples were analysed on a Spectro CirosCCD (Spectro Analysis) Inductively-Coupled Plasma-Atomic Emission Spectrophotometer. Levels of Ru and Fe in the samples were determined by a calibration curve using multi-element standard solutions containing 0.1, 0.2, 5 and 10 mg L⁻¹ Ru and Fe.

Membrane damage ATP release assays

Loss of *E. coli* membrane integrity following 4⁺ exposure was determined by leakage of ATP, an intracellular marker, from *E. coli* cells.⁵⁵ Levels of extracellular ATP of *E. coli* grown with or without 4⁺ were determined as follows. *E. coli* EC958 cells were grown to mid-exponential phase in GDMM and then 4⁺ (0 – 1.6 μ M) was added to cultures. Immediately prior to, and at time-intervals after 4⁺ addition, samples of cell culture were harvested by centrifugation at 15, 000 x g for 5 min at 4 °C to remove cells. Supernatants were recovered and retained at – 20 °C for ATP analysis. ATP analysis was conducted using the bioluminescence-based Molecular Probes' ATP Determination kit (Invitrogen, Fisher Scientific). The levels of ATP in supernatants were derived via a standard curve of ATP standards from 1 nM - 1 μ M. Luminescence measurements of ATP standards and culture supernatants were measured in duplicate on a Lumat³ Luminometer (Berthold Technologies, UK).

Single stain microscopy

Preparing the culture

An overnight culture of bacteria (EC958) was grown in LB. The cells were washed (x2) and resuspended in GDMM. The cells were diluted to OD₆₀₀-0.05 and grown to OD-0.3-0.4 in GDMM (50 mL). 1 mL of culture was harvested, and the compound added at MIC concentration. 1 mL cultures were then harvested at 5, 10, 20 and 60 minutes. The bacteria were pelleted (centrifuge, 14,000 RPM, 90 seconds), and supernatant removed. The pellet was suspended in fixant (16% paraformaldehyde in PBS, 500 μ L) and Milli-Q water (500 μ L) and placed on a rotary wheel at room temperature for 30 minutes. The samples were washed in PBS and frozen as a pellet.

Preparing the slides

Coverslips were sonicated in 1M KOH for 15 minutes, then coated in polylysine solution for 30 minutes. The pellets were suspended in 5 μ L of a SlowFade Gold Antifade Mountant (ThermoFisher). The suspension was mounted onto the slide and the coverslip placed on top. Slides were imaged using the structured illumination (SIM) microscope. Imaging was done using the 1514 immersion oil, and mol_probes microscope setting. A phase contrast image was taken (DIC) and the 450 nm laser used to excite the compound, luminescent images were collected in the A568 channel. OMX SI reconstruction was performed on images. Images were processed and analyzed using FIJI Image J software – the SIM plugin was used to perform a 16-bit conversion.

NHS ester-405 counterstain

Initial pellets were grown and fixed as before. After fixing the sample was washed with PBS. Cells were resuspended in PBS (250 μ L), NHS-ester 405 was added (50 μ g/mL). Samples were incubated on a rotary wheel at room temperature for 5 minutes. Cells were pelleted (14,000 RPM, 90 seconds) and washed with PBS (3 washes). Cell suspensions were mounted as previous. Laser 405 nm, emission filter DAPI. OMX SI reconstruction and OMX SI image registration was performed on the images, and the images were processed and analyzed using the FIJI Image J software.

HyVolution and STED microscopy

Initial pellets were grown, fixed and mounted as previously discussed. Imaging was done on a commercial LEICA SP8 3X gSTED SMD confocal microscope (Leica Microsystems, Mannheim, Germany), with capability of also performing high-resolution microscopy via Hyvolution. The STED nanoscope is equipped with 3 depletion lines and it is also equipped with a 3D STED additional vortex to obtain higher spatially resolved images in XY and Z (enhanced axial super-resolution). The excitation laser beam consisted of a pulsed (80MHz) super-continuum white light laser (WLL). For a cleaner emission the excitation lines had a clean-up notch filter (NF) in the optical pathway. Images were taken using the pulsed White Light Laser (WLL) line excitation at 475 nm, and recording the emission between 600-650 nm. The pulsed STED images were taken with a pulsed 775 nm depletion Laser, again in every case the respective NF were in place. The objective employed was a Leica 100x/1.4 NA oil objective. The pinhole was set at one Airy unit. The gated HyD detectors were set with the gated option on and the temporal gated selected was from 2 to 6.5ns. For the 3D STED images, the depletion lasers were split in two, the second vortex was set at 65%. For the Hyvolution mode, the pinhole was set at 0.5 Airy units. Every image was acquired in the Leica HyD photon counting detectors.

The Hyvolution technology, developed by Leica microsystems with the deconvolution Huygens software company (SVI, Netherlands), employs a reduced pinhole size at the detection pathway for the image acquisition. The image is later deconvoluted using the Huygens software package. The deconvolution software uses the raw data information from the Leica acquisition files for an optimal deconvolution, for 3D objects we employed a theoretical PSF, as it automatically counteracts the possible aberrations caused for in-depth imaging. The single plane images were deconvolved with a theoretical calculated PSF provided by the software and by an experimentally calculated PSF from fluorescent beads, in both cases no apparent difference was observed. Image analysis and deconvolution of STED images resolved the localisation and distribution of the organometallic dye at the bacteria. As expected the images had low intensity counts; to maximise signal-to-noise we deconvolved the images using a commercially available software (Huygens package software, SVI, Netherlands). To quantify the background level of noise we used either an automated quantification provided by the software or a manual by means of computing the averaged background intensity from regions outside the cell. We obtained better results with the manual process. For the deconvolution we used 40 iterations, a signal to noise ratio of 15, and the classical maximum likelihood estimation method provided by the software. The quantification of the resolution obtained at specific position on the bacteria was done employing the full width at half maximum (FWHM) method. The intensity line profiles over a distance drawn at the bacteria were represented using OriginPro ((OriginLab Corporation, Northampton, MA, U.S.A.)), and the calculation was done by fitting the peaks to a Gaussian function. The same software package was used for data plotting and analysis. The data was represented in

form of normalized distribution population. The figures have been developed employing the free open source software Inkscape. The surface rendered images were obtained by Huygens Professional, LAX software (Leica SP8) to generate the surface rendered 3D STED images, and the orthogonal views, the rest of the images have been post processed with Fiji (ImageJ; NIH).

Galleria Mellonella toxicity screen

TruLarv™ Galleria Mellonella were used for this study to ensure they were reared without antibiotics and were all a similar weight. For each compound concentration 7 Galleria were used, and for the control 15 Galleria were used. Insects were injected on the initial day with 10 μ L of the correct concentration stock solution of 4⁺ or water (control) into their left pro-leg. Once injected Galleria were stored in a petri dish containing filter paper and incubated at 37.5 °C. Three analysis tests were conducted at 0, 24, 48, 72, 96 and 120 hours. Activity scores were recorded: 0-no movement, 1-corrects itself, 2-movement on stimulation, 3-movement without stimulation. Live/dead scores recorded to produce percentage survival curves. Melanisation was scored on a scale of 0-4: 0 – completely black, 1 – black spots, 2- tail/line black and 4 – none. Cocoon formation was not observed in this case. At the end of the toxicity screen Galleria were disposed of in a humane manner.

Transmission electron microscopy

Cell pellets up until fixation were prepared in the same way as the single-stain super-resolution microscopy samples. The cells were fixed using 3% glutaraldehyde. Cells were dehydrated using a series of ethanol washes (70 – 100% ethanol) and TEM samples sectioned in Araldite resin by microtome. Samples were examined on a FEI Tecnai instrument operating at 80 kV equipped with a Gatan 1 K CCD camera. Images were processed and analyzed using FIJI Image J software.

BacLight™ membrane polarisation assay

Membrane polarisation was studied using the Mol Probes BacLight™ polarisation kit. Overnight cultures of EC958 were grown as previously described. Cells were grown to the exponential phase (OD: 0.4) in GDMM at 37.5 °C. One solution of bacteria was treated with 4⁺ (1.6 μ M) and incubated at for 60 minutes 37.5 °C. The other solution was the untreated control. OD was measured and cells were diluted in PBS to a final concentrations of 10⁶ CFU/mL. Four flow cytometry tubes were prepared to sample. A,B: 1 mL of the cells treated with 4⁺ and the unstained control were incubated with 10 μ L of DiOC₂(3) (3 mM) for 30 minutes in the dark in separate flow cytometry tubes. The membrane polarisation positive control tube was prepared with 10 μ L of carbonyl cyanide 3-chlorophenylhydrazone (CCCP) (500 μ M) 10 μ L of DiOC₂(3) (3 mM), the cells were incubated for 30 minutes in the dark before reading. In addition a fourth control was prepared in the absence of DiOC₂(3) on 4⁺ stained cells. Readings were taken on an LSR II flow cytometer and data analysed using the FlowJo software.

ASSOCIATED CONTENT

Supplementary Data, Instrumentation. This material is available free of charge *via* the Internet at <http://pubs.acs.org>.

AUTHOR INFORMATION

Corresponding Authors

* hannahsoutham@gmail.com; r.poole@sheffield.ac.uk; james.thomas@sheffield.ac.uk

ACKNOWLEDGMENT

KS is grateful to the BBRSC for a PhD studentship through the White Rose Structural Biology DTP. HMS and RKP also acknowledge support from a BBSRC grant (BB/M022579/1). Imaging work was performed at the Wolfson Light Microscopy Facility, using a DeltaVision/ GE OMX optical microscope, funded by MRC grant MK/K0157531/1. Imaging work was assisted by Christa Walther of the Department of MBB, University of Sheffield. ICP-AES was performed by Neil Bramall at the Faculty of Science Mass Spectrometry Centre, University of Sheffield. TEM was assisted by Christopher Hill of the Department of MBB at the University of Sheffield.

REFERENCES

- Erkkila, K. E.; Odom, D. T.; Barton, J. K. Recognition and Reaction of Metallointercalators with DNA. *Chem. Rev.* **1999**, *99*, 2777–2796.
- Metcalfe, C.; Thomas, J. A. Kinetically Inert Transition Metal Complexes That Reversibly Bind to DNA. *Chem Soc Rev* **2003**, *32*, 215–10.
- Keene, F. R.; Smith, J. A.; Collins, J. G. Metal Complexes as Structure-Selective Binding Agents for Nucleic Acids. *Coord. Chem. Rev.* **2009**, *253*, 2021–2035.
- McKinley, A. W.; Lincoln, P.; Tuite, E. M. Environmental Effects on the Photophysics of Transition Metal Complexes with Dipyrido[2,3-a:3',2'-c]Phenazine (Dppz) and Related Ligands. *Coord Chem Rev* **2011**, *255*, 2676–2692.
- Gill, M. R.; Thomas, J. A. Ruthenium(II) Polypyridyl Complexes and DNA--From Structural Probes to Cellular Imaging and Therapeutics. *Chem Soc Rev* **2012**, *41*, 3179–3192.
- Komor, A. C.; Barton, J. K. The Path for Metal Complexes to a DNA Target. *Chem. Commun.* **2013**, *49*, 3617–3630.
- Poynton, F. E.; Bright, S. A.; Blasco, S.; Williams, D. C.; Kelly, J. M.; Gunnlaugsson, T. The Development of Ruthenium(II) Polypyridyl Complexes and Conjugates for *In Vitro* Cellular and *In Vivo* Applications. *Chem Soc Rev* **2017**, *36*, 1–51.
- Antonarakis, E. S.; Emadi, A. Ruthenium-Based Chemotherapeutics: Are They Ready for Prime Time? *Cancer Chemother Pharmacol* **2010**, *66*, 1–9.
- Shi, G.; Monro, S.; Hennigar, R.; Colpitts, J.; Fong, J.; Kasimova, K.; Yin, H.; DeCoste, R.; Spencer, C.; Chamberlain, L.; Mandel, A.; Lilge, L. & Mcfarland, S. Ru(II) Dyads Derived From A-Oligothiophenes: a New Class of Potent and Versatile Photosensitizers for PDT. *Coord Chem Rev* **2015**, *282-283*, 127–138.
- Knoll, J. D.; Turro, C. Control and Utilization of Ruthenium and Rhodium Metal Complex Excited States for Photoactivated Cancer Therapy. *Coord. Chem. Rev.* **2015**, *282-283*, 110–126.
- Heinemann, F.; Karges, J.; Gasser, G. Critical Overview of the Use of Ru(II) Polypyridyl Complexes as Photosensitizers in One-Photon and Two-Photon Photodynamic Therapy. *Acc. Chem. Res.* **2017**, *50*, 2727–2736.
- Zeng, L.; Gupta, P.; Chen, Y.; Wang, E.; Ji, L.; Chao, H.; Chen, Z.-S. The Development of Anticancer Ruthenium(II) Complexes: From Single Molecule Compounds to Nanomaterials. *Chem Soc Rev* **2017**, *46*, 5771–5804.
- Dwyer, F. P.; Gyarfás, E. C.; Rogers, W. P.; Koch, J. H. Biological Activity of Complex Ions. *Nature* **1952**, *170*, 190–191.
- Brandt, W. W.; Dwyer, F. P.; Gyarfás, E. D. Chelate Complexes of 1, 10-Phenanthroline and Related Compounds. *Chem. Rev.* **1954**, *54*, 959–1017.
- Dwyer, F. P.; Reid, I. K.; Shulman, A.; Laycock, G. M.; Dixon, S. The Biological Actions of 1,10-Phenanthroline and 2,2'-Bipyridine Hydrochlorides, Quaternary Salts and Metal Chelates and Related Compounds. 1. Bacteriostatic Action on Selected Gram-Positive, Gram-Negative and Acid-Fast Bacteria. *Aust J Exp Biol Med Sci* **1969**, *47*, 203–218.
- Davies, J.; Davies, D. Origins and Evolution of Antibiotic Resistance. *Microbiol Mol Biol Rev* **2010**, *74*, 417–433.
- Silver, L. L. Challenges of Antibacterial Discovery. *Clinical Microbiology Reviews* **2011**, *24*, 71–109.
- Holmes, A. H.; Moore, L. S. P.; Sundsfjord, A.; Steinbakk, M.; Regmi, S.; Karkey, A.; Guerin, P. J.; Piddock, L. J. V. Understanding the Mechanisms and Drivers of Antimicrobial Resistance. *Lancet* **2016**, *387*, 176–187.
- Fridman, M. Catalyst: the Role of Chemistry in Delivering the Next Antimicrobial Drugs. *Chem* **2017**, *3*, 8–10.
- Bolhuis, A.; Hand, L.; Marshall, J. E.; Richards, A. D.; Rodger, A.; Aldrich-Wright, J. Antimicrobial Activity of Ruthenium-Based Intercalators. *European Journal of Pharmaceutical Sciences* **2011**, *42*, 313–317.
- Kumar, S. V.; Scottwell, S. Ø.; Waugh, E.; McAdam, C. J.; Hanton, L. R.; Brooks, H. J. L.; Crowley, J. D. Antimicrobial Properties of Tris(Homoleptic) Ruthenium(II) 2-Pyridyl-1,2,3-Triazole “Click” Complexes Against Pathogenic Bacteria, Including Methicillin-Resistant *Staphylococcus Aureus* (MRSA). *Inorg Chem* **2016**, *55*, 9767–9777.
- Southam, H. M.; Butler, J. A.; Chapman, J. A.; Poole, R. K. The Microbiology of Ruthenium Complexes. *Adv. Microb. Physiol.* **2017**, *71*, 1–96.
- Mårtensson, A. K. F.; Bergentall, M.; Tremaroli, V.; Lincoln, P. Diastereomeric Bactericidal Effect of Ru(Phenanthroline) 2dipyridophenazine. *Chirality* **2016**, *28*, 713–720.
- Li, F.; Collins, J. G.; Keene, F. R. Ruthenium Complexes as Antimicrobial Agents. *Chem Soc Rev* **2015**, *44*, 2529–2542.
- Li, F.; Mulyana, Y.; Feterl, M.; Warner, J. M.; Collins, J. G.; Keene, F. R. The Antimicrobial Activity of Inert Oligonuclear Polypyridylruthenium(II) Complexes Against Pathogenic Bacteria, Including MRSA. *Dalton Trans* **2011**, *40*, 5032.
- Pandrala, M.; Li, F.; Feterl, M.; Mulyana, Y.; Warner, J. M.; Wallace, L.; Keene, F. R.; Collins, J. G. Chlorido-Containing Ruthenium(II) and Iridium(III) Complexes as Antimicrobial Agents. *Dalton Trans* **2013**, *42*, 4686.
- Li, F.; Harry, E. J.; Bottomley, A. L.; Edstein, M. D.; Birrell, G. W.; Woodward, C. E.; Keene, F. R.; Collins, J. G. Dinuclear Ruthenium(II) Antimicrobial Agents That Selectively Target Polysomes *In Vivo*. *Chem. Sci.* **2014**, *5*, 685–693.
- Weber, D. K.; Sani, M.-A.; Downton, M. T.; Separovic, F.; Keene, F. R.; Collins, J. G. Membrane Insertion of a Dinuclear Polypyridylruthenium(II) Complex Revealed by Solid-State NMR and Molecular Dynamics Simulation: Implications for Selective Antibacterial Activity. *J. Am. Chem. Soc.* **2016**, *138*, 15267–15277.
- Gorle, A. K.; Feterl, M.; Warner, J. M.; Primrose, S.; Constantinoiu, C. C.; Keene, F. R.; Collins, J. G. Mononuclear Polypyridylruthenium(II) Complexes with High Membrane Permeability in Gram-Negative Bacteria-in Particular *Pseudomonas Aeruginosa*. *Chem. Eur. J.* **2015**, *21*, 10472–10481.
- World Health Organization. *Antimicrobial Resistance: Global Report on Surveillance*; 2014.
- Tommasi, R.; Brown, D. G.; Walkup, G. K.; Manchester, J. I.; Miller, A. A. ESKAPEing the Labyrinth of Antibacterial Discovery. *Nat Rev Drug Discov* **2015**, *14*, 529–542.
- World Health Organization. *Global Priority List of Antibiotic-Resistant Bacteria to Guide Research, Discovery, and Development of New Antibiotics*; Geneva: World Health Organization, 2017.
- Butler, M. S.; Blaskovich, M. A.; Cooper, M. A. Antibiotics in the Clinical Pipeline at the End of 2015. *J. Antibiot.* **2017**, *70*, 3–24.
- Payne, D. J.; Gwynn, M. N.; Holmes, D. J.; Pompliano, D. L. Drugs for Bad Bugs: Confronting the Challenges of Antibacterial Discovery. *Nat Rev Drug Discov* **2006**, *6*, 29–40.

- (35) Singh, S. B.; Young, K.; Silver, L. L. What Is an “Ideal” Antibiotic? Discovery Challenges and Path Forward. *Biochemical Pharmacology* **2017**, *133*, 63–73.
- (36) Gill, M. R.; Garcia-Lara, J.; Foster, S. J.; Smythe, C.; Battaglia, G.; Thomas, J. A. A Ruthenium(II) Polypyridyl Complex for Direct Imaging of DNA Structure in Living Cells. *Nat Chem* **2009**, *1*, 662–667.
- (37) Gill, M. R.; Cecchin, D.; Walker, M. G.; Mulla, R. S.; Battaglia, G.; Smythe, C.; Thomas, J. A. Targeting the Endoplasmic Reticulum with a Membrane-Interactive Luminescent Ruthenium(II) Polypyridyl Complex. *Chem. Sci.* **2013**, *4*, 4512–4519.
- (38) Wragg, A.; Gill, M. R.; Turton, D.; Adams, H.; Roseveare, T. M.; Smythe, C.; Su, X.; Thomas, J. A. Tuning the Cellular Uptake Properties of Luminescent Heterobimetallic Iridium(III)-Ruthenium(II) DNA Imaging Probes. *Chem. Eur. J.* **2014**, *20*, 14004–14011.
- (39) Ramu, V.; Gill, M. R.; Jarman, P. J.; Turton, D.; Thomas, J. A.; Das, A.; Smythe, C. A Cytostatic Ruthenium(II)-Platinum(II) Bis(Terpyridyl) Anticancer Complex That Blocks Entry Into S Phase by Up-Regulating P27 KIP1. *Chem. Eur. J.* **2015**, *21*, 9185–9197.
- (40) Walker, M. G.; Jarman, P. J.; Gill, M. R.; Tian, X.; Ahmad, H.; Reddy, P. A. N.; McKenzie, L.; Weinstein, J. A.; Meijer, A. J. H. M.; Battaglia, G.; *et al.* A Self-Assembled Metallo-macrocyclic Singlet Oxygen Sensitizer for Photodynamic Therapy. *Chem. Eur. J.* **2016**, *22*, 5996–6000.
- (41) Gill, M. R.; Jarman, P. J.; Halder, S.; Walker, M. G.; Saeed, H. K.; Thomas, J. A.; Smythe, C.; Ramadan, K.; Vallis, K. A. A Three-in-One-Bullet for Oesophageal Cancer: Replication Fork Collapse, Spindle Attachment Failure and Enhanced Radiosensitivity Generated by a Ruthenium(II) Metallo-Intercalator. *Chem. Sci.* **2018**, *9*, 841–849.
- (42) Bolger, J.; Gourdon, A.; Ishow, E.; Launay, J.-P. Mononuclear and Binuclear Tetrapyrido [3, 2-a: 2', 3'-C: 3", 2"-H: 2"', 3'''-'''] Phenazine (Tpphz) Ruthenium and Osmium Complexes. *Inorg Chem* **1996**, *35*, 2937–2944.
- (43) Li, S. P.-Y.; Tang, T. S.-M.; Yiu, K. S.-M.; Lo, K. K.-W. Cyclometalated Iridium(III)-Polyamine Complexes with Intense and Long-Lived Multicolor Phosphorescence: Synthesis, Crystal Structure, Photophysical Behavior, Cellular Uptake, and Transfection Properties. *Chem. Eur. J.* **2012**, *18*, 13342–13354.
- (44) Horobin, R. W.; Rashid-Doubell, F.; Pediani, J. D.; Milligan, G. Predicting Small Molecule Fluorescent Probe Localization in Living Cells Using QSAR Modeling. 1. Overview and Models for Probes of Structure, Properties and Function in Single Cells. *Biotechnol & Histochemistry* **2013**, *88*, 440–460.
- (45) Flatley, J.; Barrett, J.; Pullan, S. T.; Hughes, M. N.; Green, J.; Poole, R. K. Transcriptional Responses of Escherichia Colito S-Nitrosoglutathione Under Defined Chemostat Conditions Reveal Major Changes in Methionine Biosynthesis. *J. Biol. Chem.* **2005**, *280*, 10065–10072.
- (46) Willmann, J. K.; van Bruggen, N.; Dinkelborg, L. M.; Gambhir, S. S. Molecular Imaging in Drug Development. *Nat Rev Drug Discov* **2008**, *7*, 591–607.
- (47) Bullen, A. Microscopic Imaging Techniques for Drug Discovery. *Nat Rev Drug Discov* **2008**, *7*, 54–67.
- (48) Lang, P.; Yeow, K.; Nichols, A.; Scheer, A. Cellular Imaging in Drug Discovery. *Nat Rev Drug Discov* **2006**, *5*, 343–356.
- (49) Sreedharan, S.; Gill, M. R.; Garcia, E.; Saeed, H. K.; Robinson, D.; Byrne, A.; Cadby, A.; Keyes, T. E.; Smythe, C.; Pellett, P.; *et al.* Multimodal Super-Resolution Optical Microscopy Using a Transition-Metal-Based Probe Provides Unprecedented Capabilities for Imaging Both Nuclear Chromatin and Mitochondria. *J. Am. Chem. Soc.* **2017**, *139*, 15907–15913.
- (50) Gustafsson, M. Surpassing the Lateral Resolution Limit by a Factor of Two Using Structured Illumination Microscopy. *J. Microsc* **2000**, *198*, 82–87.
- (51) Fiolka, R.; Shao, L.; Rego, E. H.; Davidson, M. W.; Gustafsson, M. G. L. Time-Lapse Two-Color 3D Imaging of Live Cells with Doubled Resolution Using Structured Illumination. *Proc. Natl. Acad. Sci. U.S.A* **2012**, *109*, 5311–5315.
- (52) Blom, H.; Widengren, J. Stimulated Emission Depletion Microscopy. *Chem. Rev.* **2017**, *117*, 7377–7427.
- (53) Clausen, M. P.; Galiani, S.; Bernardino de la Serna, J. B. de L.; Fritzsche, M.; Chojnacki, J.; Gehmlich, K.; Lagerholm, B. C.; Eggeling, C. Pathways to Optical STED Microscopy. **2014**, *1*, 1–12.
- (54) Hell, S. W. Far-Field Optical Nanoscopy. *Science* **2007**, *316*, 1153–1158.
- (55) O'Neill, A. J.; Miller, K.; Oliva, B.; Chopra, I. Comparison of Assays for Detection of Agents Causing Membrane Damage in Staphylococcus Aureus. *J. Antimicrob. Chemother.* **2004**, *54*, 1127–1129.
- (56) Shapiro, H. M. Membrane Potential Estimation by Flow Cytometry. *Methods* **2000**, *21*, 271–279.
- (57) Brochado, A. R.; Telzerow, A.; Bobonis, J.; Banzhaf, M.; Mateus, A.; Selkrig, J.; Huth, E.; Bassler, S.; Zamarreño Beas, J.; Zietek, M.; *et al.* Species-Specific Activity of Antibacterial Drug Combinations. *Nature* **2018**, *559*, 259–263.
- (58) Kemp, M. W.; Massey, R. C. The Use of Insect Models to Study Human Pathogens. *Drug Discovery Today: Disease Models* **2007**, *4*, 105–110.
- (59) Maguire, R.; Duggan, O.; Kavanagh, K. Evaluation of *Galleria Mellonella* Larvae as an in Vivo Model for Assessing the Relative Toxicity of Food Preservative Agents. *Cell Biology and Toxicology* **2016**, *32*, 1–8.
- (60) Allegra, E.; Titball, R. W.; Carter, J.; Champion, O. L. *Galleria Mellonella* Larvae Allow the Discrimination of Toxic and Non-Toxic Chemicals. *Chemosphere* **2018**, *198*, 469–472.
- (61) Nussbaum, von, F.; Brands, M.; Hinzen, B.; Weigand, S.; Häbich, D. Antibacterial Natural Products in Medicinal Chemistry—Exodus or Revival? *Angew. Chem. Int. Ed.* **2006**, *45*, 5072–5129.
- (62) Shore, C. K.; Coukell, A. Roadmap for Antibiotic Discovery. *Nat Microbiol* **2016**, *1*, 16083.
- (63) Gwynn, M. N.; Portnoy, A.; Rittenhouse, S. F.; Payne, D. J. Challenges of Antibacterial Discovery Revisited. *Ann N Y Acad Sci* **2010**, *1213*, 5–19.
- (64) Brown, E. D.; Wright, G. D. Antibacterial Drug Discovery in the Resistance Era. *Nature* **2016**, *529*, 336–343.
- (65) Cooper, M. A. A Community-Based Approach to New Antibiotic Discovery. *Nat Rev Drug Discov* **2015**, *14*, 587–588.
- (66) Pawlowski, A. C.; Johnson, J. W.; Wright, G. D. Evolving Medicinal Chemistry Strategies in Antibiotic Discovery. *Current Opinion in Biotechnology* **2016**, *42*, 108–117.
- (67) Hurdle, J. G.; O'Neill, A. J.; Chopra, I.; Lee, R. E. Targeting Bacterial Membrane Function: an Underexploited Mechanism for Treating Persistent Infections. *Nat. Rev. Microbiol.* **2011**, *9*, 62–75.
- (68) O'Shea, R.; Moser, H. E. Physicochemical Properties of Antibacterial Compounds: Implications for Drug Discovery. *J. Med. Chem.* **2008**, *51*, 2871–2878.
- (69) Brown, D. G.; May-Dracka, T. L.; Gagnon, M. M.; Tommasi, R. Trends and Exceptions of Physical Properties on Antibacterial Activity for Gram-Positive and Gram-Negative Pathogens. *J. Med. Chem.* **2014**, *57*, 10144–10161.
- (70) Richter, M. F.; Drown, B. S.; Riley, A. P.; Garcia, A.; Shirai, T.; Svec, R. L.; Hergenrother, P. J. Predictive Compound Accumulation Rules Yield a Broad-Spectrum Antibiotic. *Nature* **2017**, *545*, 299–304.
- (71) Smith, P. A.; Koehler, M. F. T.; Girgis, H. S.; Yan, D.; Chen, Y.; Chen, Y.; Crawford, J. J.; Durk, M. R.; Higuchi, R. I.; Kang, J.; *et al.* Optimized Arylomycins Are a New Class of Gram-Negative Antibiotics. *Nature* **2018**, *561*, 189–194.

- (72) Sullivan, B. P.; SALMON, D. J.; Meyer, T. J. Mixed Phosphine 2,2'-Bipyridine Complexes of Ruthenium. *Inorg Chem* **2002**, *17*, 3334–3341.
- (73) Rajput, C.; Rutkaite, R.; Swanson, L.; Haq, I.; Thomas, J. A. Dinuclear Monointercalating RuII Complexes That Display High Affinity Binding to Duplex and Quadruplex DNA. *Chem. Eur. J.* **2006**, *12*, 4611–4619.
- (74) Sangster, J. Octanol-Water Partition Coefficients of Simple Organic Compounds. *Journal of Physical and Chemical Reference Data* **1989**, *18*, 1111–1229.
- (75) Forde, B. M.; Ben Zakour, N. L.; Stanton-Cook, M.; Phan, M.-D.; Totsika, M.; Peters, K. M.; Chan, K. G.; Schembri, M. A.; Upton, M.; Beatson, S. A. The Complete Genome Sequence of Escherichia Coli EC958: a High Quality Reference Sequence for the Globally Disseminated Multidrug Resistant E. Coli O25b:H4-ST131 Clone. *PLoS ONE* **2014**, *9*, e104400–e104413.
- (76) I.T. Paulsen, L. Banerjee, G.S. Myers, K.E. Nelson, R. Seshadri, T.D. Read, D.E. Fouts, J.A. Eisen, S. R. Gill, J.F. Heidelberg, H. Tettelin, R. J. Dodson, L. Umayam, L. Brinkac, M. Beanan, S. Daugherty, R. T. Deboy, S. Durkin, J. Kolonay, R. Madupu, W. Nelson, J. Vamathevan, B. Tran, J. Upton, T. Hansen, J. Shetty, H. Khouri, T. Utterback, D. Radune, K. A. Ketchup, B. A. Dougherty, C. M. Fraser. Role of Mobile DNA in the Evolution of Vancomycin-Resistant Enterococcus Faecalis. *Science* **2003**, *299*, 2071–2074.